Tsukahara and Takada *Earth, Planets and Space* (2018) 70:52
https://doi.org/10.1186/s40623-018-0816-6

Earth, Planets and Space

EXPRESS LETTER

Open Access

Aseismic fold growth in southwestern Taiwan detected by InSAR and GNSS

Kotaro Tsukahara[1*] and Youichiro Takada[2]

Abstract

We report very rapid and aseismic fold growth detected by L-band InSAR images and GNSS data in southwestern Taiwan where is characterized by high convergence rate and low seismicity. Six independent interferograms acquired from ascending orbit during 2007–2011 commonly indicate large line-of-sight (LOS) shortening. For descending orbit, one interferogram spanning 21 months also indicates the LOS shortening at the same location. After removing long-wavelength noise and height-dependent phase component from these interferograms using GNSS velocity field and DEM, we obtained the quasi-vertical and the quasi-east velocity fields. We found very rapid uplift (quasi-vertical movement) in the fold and thrust belt to the east of the Tainan city. The uplifted area stretches about 25 km in the N–S direction and about 5 km in the E–W direction. At the southern part of the uplifted area, the uplift rate obtained by InSAR is consistent with that measured by the leveling survey, which takes 18 mm/year at a maximum. On the other hand, at the northern part, the maximum uplift rate detected by InSAR reaches up to 37 mm/year, more than twice as large as the rate along the levelling route. Judging from very low seismicity in this region, the severe crustal deformation we detected with InSAR is aseismic. At the eastern flank of the uplifted area, we found a sharp discontinuity in the uplift rate from the ALOS/PALSAR interferometry, and a sharp discontinuity in the amount of uplift in response to the 2016 Meinong earthquake (M6.4) from ALOS-2/PALSAR2 interferometry, which implies the existence of a shallow active fault. The stable slip of this active fault would be due to the high pore fluid pressure reported in this region. The aseismic uplift before the Meinong earthquake would be mainly due to the mud diapirs at the depth, which is perturbed by the aseismic movement of the shallow active fault.

Keywords: Aseismic deformation, Taiwan, InSAR, GNSS

Introduction

The collision between the Luzon island arc and the Eurasian continental margin brings about large-scale deformation in Taiwan (e.g., Rau and Wu 1995; Takada et al. 2007). Taiwan is one of the fastest growing orogens in the world, which enables us to test many ideas of landscape evolution processes. Southwestern part of Taiwan is characterized by rapid interplate convergence as well as low seismic activity (Fig. 1). We may expect the existence of rapid aseismic deformation, which, in general, can be caused by plate interface locking, postseismic deformation of the past earthquakes, and so forth. Interferometric Synthetic Aperture Radar (InSAR) is a powerful tool to grasp the short-wavelength deformation (e.g., Massonnet et al. 1993) which cannot be detected by nationwide GNSS survey. For southwest Taiwan, previous studies using C-band SAR data reported crustal deformation in and around urban areas (Fruneau et al. 2001; Huang et al. 2009; Huang et al. 2016a), but not successful in the mountainous areas. In this study, we use SAR data of L-band satellites (ALOS and ALOS-2) to obtain coherent images even in the mountainous region covered by dense vegetation. The L-band data are more sensitive to ionospheric and tropospheric disturbances than C- and X-band data. To avoid this disadvantage, we use GNSS data to correct the interferograms. The ALOS image acquisition from descending orbit is very sparse in Taiwan, to which InSAR time series analysis (e.g., Ferretti et al. 2001; Berardino et al. 2002) is not applicable for

*Correspondence: k.tsukahara@frontier.hokudai.ac.jp
[1] Department of Natural History Sciences, Hokkaido University, N10W8, Kita-ku, Sapporo 060-0810, Japan
Full list of author information is available at the end of the article

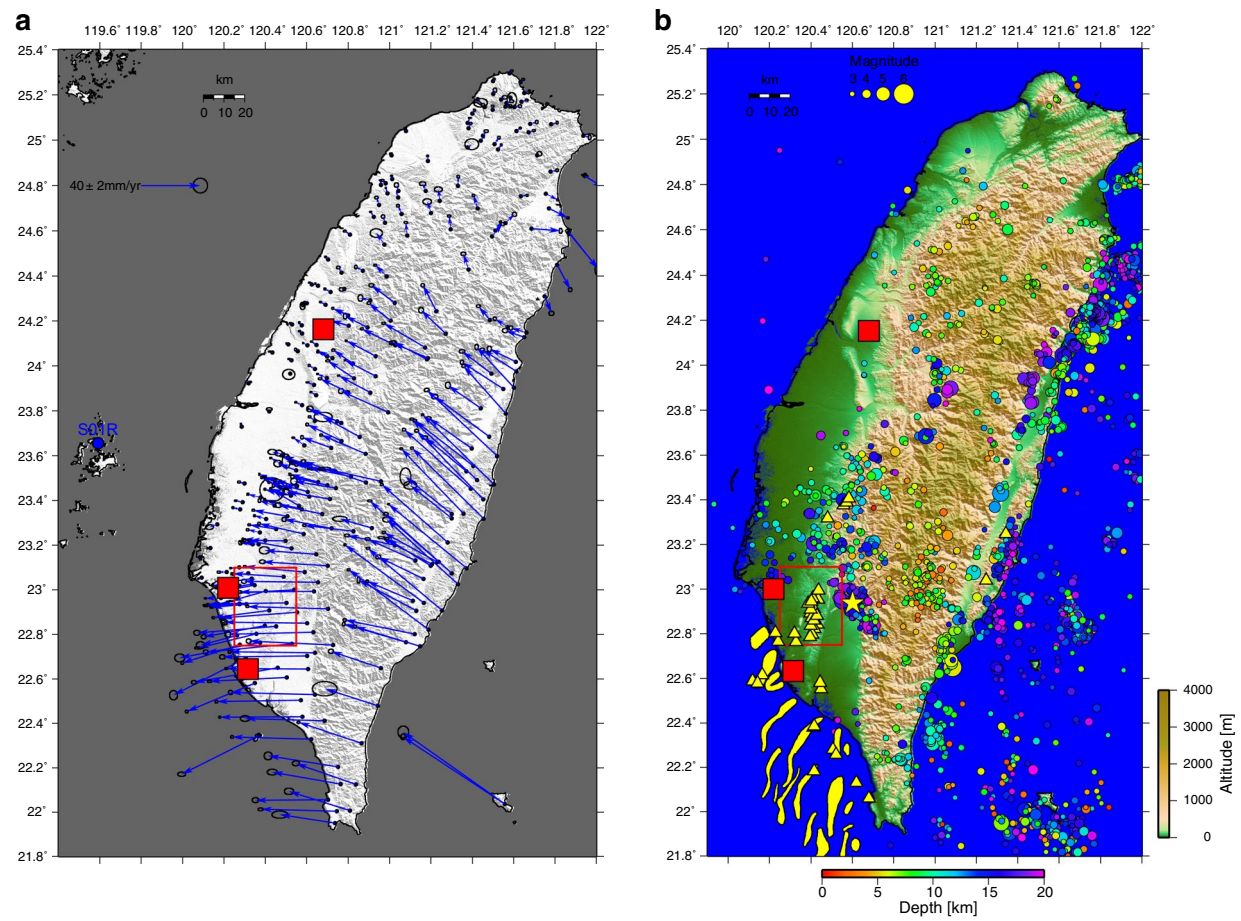

Fig. 1 Crustal deformation and seismicity in Taiwan. Red rectangle denotes the study area. Red squares stand for, from north to south, Taichung, Tainan, and Kaohsiung, respectively. **a** Horizontal velocity field with respect to S01R (Paisha, Penghu) obtained by GNSS measurements (Tsai et al. 2015). Ellipsoid indicates 95% confidence interval. **b** Hypocentral distribution of shallow earthquakes provided by Central Weather Bureau. Radius and color of circles indicate magnitude and depth of earthquakes, respectively. Yellow areas indicate mud diapirs (Lin et al. 2009). Yellow triangles indicate mud volcanoes (Sun et al. 2010). Yellow star indicates epicenter of the Meinong earthquake

noise reduction. Thus, the interferogram correction by GNSS is very important to estimate the uplift rates in Taiwan.

Methods

We made interferograms using ALOS/PALSAR data acquired from ascending orbit (path 447 frame 440) with GAMMA software suite (Wegmüller and Werner 1997). To remove topographic fringes, we adopted the hole-filled Shuttle Radar Topographic Mission (SRTM) 3-arc-second spacing digital elevation model (DEM) (Jarvis et al. 2008). To raise the signal-to-noise ratio, we created six interferograms taking the temporal baselines (i.e., period between master and slave dates) about 2.5 years (Table 1), by which we can keep perpendicular baseline small and avoid the effect of orbit shift (Additional file 1: Fig. S1). These interferograms are independent of each other with twelve different acquisition dates, which means no systematic errors are commonly included.

Next, we removed systematic errors included in these interferograms, following the method given by Fukushima and Hooper (2011) with some modifications. To make the corrections effective, we clipped out the area of interest (red frame in Fig. 1) from all interferograms, which increases the GNSS station density and decreases the spatial variability of atmospheric stratification. Then, we removed the height-dependent phase trend from each interferogram using the DEM. To make it precise, we temporarily estimate a bilinear phase ramp as well according to the following equation:

$$\varphi_i = a + bx_i + cy_i + fh_i \quad (1)$$

where φ_i is the phase at ith pixel located at (x_i, y_i), and h_i is the altitude derived from the DEM. The parameters

Table 1 Interferometric pairs used in this study

Satellite	Direction (Asc/Dsc)	Master (yyyy/mm/dd)	Slave (yyyy/mm/dd)	Bp (m)	Interval (days)
ALOS	Asc	2007/3/4	2009/10/25	25	965
ALOS	Asc	2007/7/20	2010/1/25	15.8	920
ALOS	Asc	2007/10/20	2010/3/12	253.9	874
ALOS	Asc	2008/1/20	2010/7/28	19.7	920
ALOS	Asc	2008/6/6	2011/1/28	66.7	966
ALOS	Asc	2008/4/21	2011/3/15	519	1058
ALOS	Dsc	2007/2/18	2008/11/23	−1037	652
ALOS-2	Asc	2015/11/26	2016/2/18	196	84
ALOS-2	Dsc	2016/1/31	2016/2/14	−203	14

Asc, ascending; Dsc, descending; Bp, perpendicular baseline

a, b, c, and f are determined in a least squares manner. Then we only subtract the height-dependent term fh_i from each interferogram. As an example, the effect of this correction for an interferogram spanning 874 days is illustrated in Fig. 2a, b, showing that the height-dependent component is very small, possibly due to low altitude of the studied area (~300 m above sea level). Next, by assuming GNSS velocity field as correct and steady, we removed the long-wavelength noise. We used the GNSS velocities provided by Tsai et al. (2015). We set Paisha, Penghu SR01 (Fig. 1) as a reference. The error of interferogram at jth GNSS station can be written as

$$d_j^{\mathrm{err}} = d_j - d_j^{\mathrm{GNSS}} \tag{2}$$

where d_j is the line-of-sight (LOS) velocity obtained by InSAR, d_j^{GNSS} is the one by GNSS, and d_j^{err} is the error defined at the GNSS stations (triangles in Fig. 2a). Then we interpolated the error d^{err} into all the pixels using bicubic spline function (Fig. 2c), by which we obtained final corrected interferogram (Fig. 2d). Comparing Fig. 2a and 2d, a remarkable long-wavelength phase trend, probably due to ionospheric disturbance, is successfully removed. We applied above correction to all the six interferograms, and the corrected interferograms are stacked to further reduce the non-systematic noise. Additional file 1: Figure S2 indicates another five ascending interferograms thus corrected. Strong similarity between these six interferograms (Fig. 2d, Additional file 1: Figure S2) indicates the effectiveness of the noise reduction by GNSS data. Such similarity also results from high signal-to-noise ratio of each interferogram with temporal baseline of ~2.5 years. Additional file 1: Figure S3 indicates the corrected interferograms with temporal baseline of 46 days and 3.5 years, respectively. Both of these are very noisy and look completely different each other. Also the temporal decorrelation is remarkable for the latter interferogram.

For descending orbit, we created only one interferogram spanning 644 days due to scare acquisition by ALOS (Table 1), to which the same correction as the ascending interferograms was applied (Additional file 1: Figure S4). Using ascending and descending interferograms thus corrected, we applied the 2.5-dimensional analysis (Fujiwara et al. 2000) to obtain quasi-vertical velocity component (Fig. 3) as well as quasi-horizontal velocity component. In the following part of this paper, we focus on the quasi-vertical component.

Results and discussion

Figure 3a shows very rapid uplift in the fold and thrust belt to the east of Tainan city (Fig. 1). The uplifted area takes N–S elongated shape, which stretches ~25 km in the N–S direction and ~5 km in the E–W direction. Judging from very low seismicity in this area (Fig. 1), we may conclude that this uplift is aseismically proceeding. As an overall trend, the uplift rate increases from south to north, and it reaches ~37 mm/year at maximum in the northern part (Fig. 3b). To elaborate the uplift pattern, we took E–W profiles of the quasi-vertical velocity field (Fig. 3b, c). Across the southern part of the uplifted area, Ching et al. (2016) reported a one-dimensional profile of uplift rate by levelling survey (Fig. 3a), showing ~18 mm/year at maximum. We compared the uplift rate detected by InSAR with that measured by the levelling survey, and demonstrated that both are consistent with each other (Fig. 3d). We further found that the uplift rate in the E–W profiles indicates a sharp discontinuity at the eastern flank of the uplifted region (shading in Fig. 3c), which is also visible in the plan view (red arrows in Fig. 3a). We interpret that this uplift rate discontinuity results from a hidden active fault steadily creeping under a certain level of shear stress. The location of this fault roughly corresponds to the Lungchuan fault, which is proposed to be a thrust fault (Huang et al. 2004; Ching et al. 2016). The

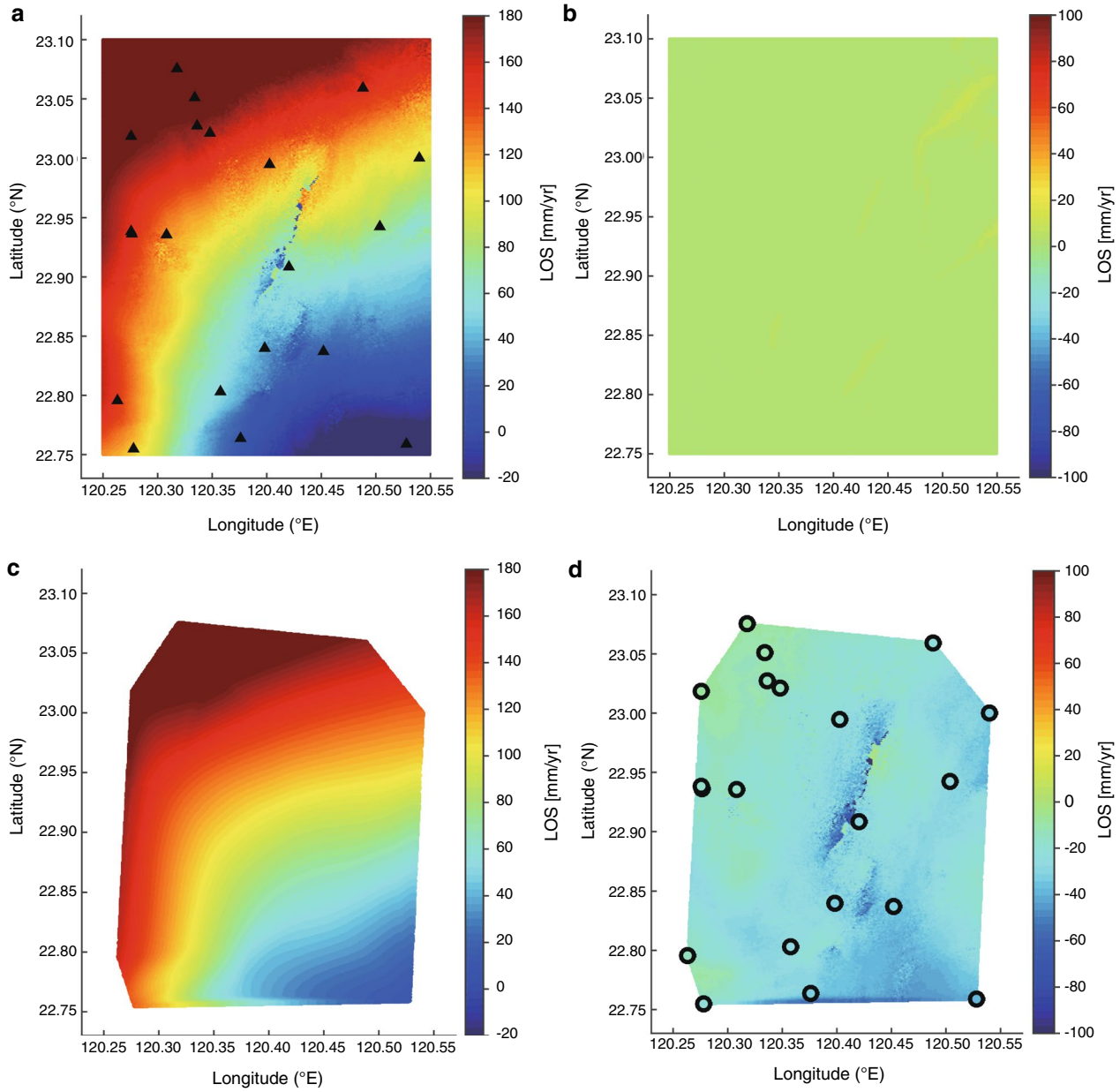

Fig. 2 Interferogram correction for the pair 20071020–20100312 spanning 874 days. Color indicates the length change velocity in the line-of-sight (LOS) direction. **a** Original interferogram. Black triangle indicates the GNSS station. **b** Height-dependent component. **c** Long-wavelength noise. **d** Corrected interferogram. Colored circle indicates the LOS velocity calculated from the GNSS data

detailed geometry and the precise location of the Lungchuan fault are poorly known, which may be improved from combination of our interferograms and field surveys in the future.

The driving force of this rapid uplift would be the growth of mud diapirs, which is widely distributed from South China Sea to the coastal area of southwest Taiwan (Doo et al. 2015; Lin et al. 2009, Huang et al. 2004) (Fig. 1b). In the uplifted area, active mud volcanoes demonstrate the existence of mud volumes at shallow depth. Ching et al. (2016) tried to construct a fault model to explain the uplift profile obtained by the levelling survey in the southern area (circles in Fig. 3a) and found it as very difficult. Instead, they proposed the mud diapirs as main driving force. In northern part, the uplift rate detected by InSAR takes much higher value than

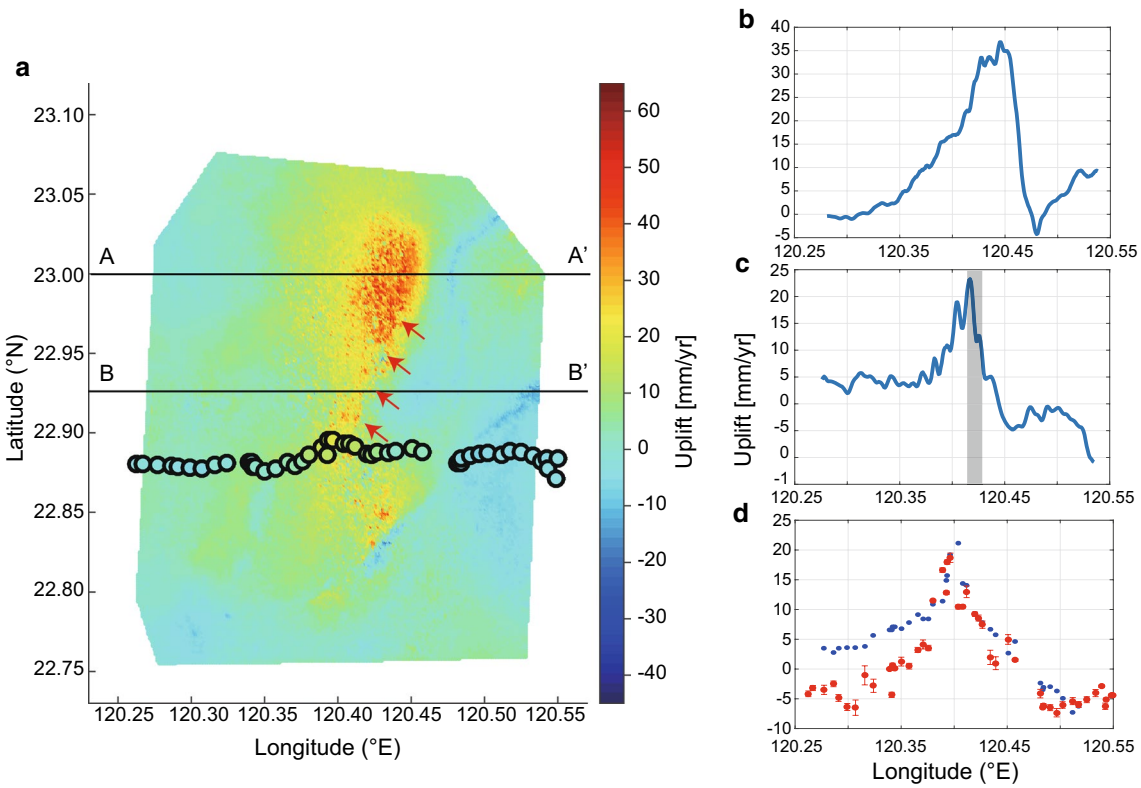

Fig. 3 Uplift rate calculated from 2.5-dimensional analysis using ALOS data. **a** Distribution of uplift rate. Colored circle stands for the uplift rate obtained from leveling survey (Ching et al. 2016). Sharp discontinuity in the uplift rate is marked by red arrows. **b** Uplift rate along the profile A–A′. **c** Uplift rate along the profile B–B′. Sharp discontinuity in the uplift rate is marked by a shading as well as in Fig. 4c. **d** Uplift rate measured by InSAR (blue dot) and leveling survey (red dot). We took 5-point running mean for the uplift rates given by InSAR in (**b**) and (**c**)

southern part, reaching 37 mm/year (Fig. 3a). This uplift rate is higher than total convergence rate across the study area (Additional file 1: Figure S5), which is unrealistic to be solely explained by fault motion. Based on the gap in the velocity field (Fig. 3), we also constructed a two-dimensional fault model using Okada's Green's function (Okada 1985). For the observed horizontal velocity, we removed very long-wavelength component which directly reflects interplate convergence (note that the reference point is S01R in Fig. 1a). We fixed the top of the fault at the surface. As shown in Additional file 1: Figure S6, the optimum fault model with a slip of 55 mm/year on a fault plane dipping 65 degrees down to the west well explains the quasi-east component (Additional file 1: Figure S6a), while we see remarkable misfit (> 15 mm/year) especially at the footwall side (right) in the quasi-vertical component (Additional file 1: Figure S6b); calculated subsidence is too large at the footwall side. Looking at the plan view (Fig. 3a), the foot wall side (east) of this reverse fault is clearly uplifted, which demonstrates that the whole area is raised by a mud diapir located at depth, and the surface offset is caused by the shallow reverse faulting that we found.

To elaborate the rheological property of the aseismic uplift area, we further analyzed the interferograms of the Meinong earthquake (Mw 6.4) that occurred about 20 km east of the uplift area (Fig. 1b) on 5 February 2016 (USGS 2016). Using SAR data acquired by ALOS-2/PALSAR2 (Table 1), we created two interferograms from ascending and descending orbits. Figure 4 shows quasi-vertical displacement associated with the Meinong earthquake. We found a gap in the amount of uplift (red arrows in Fig. 4a, shading in Fig. 4c) at the same location as the gap in the uplift rate before the earthquake (red arrows in Fig. 3a, shading in Fig. 3c). In Additional file 1: Figure S7, clear coherence loss along the gap is commonly observed in both coseismic interferogram of the Meinong earthquake and interseismic interferogram. This coherence loss indicates surface faulting of the hypothetical thrust fault. Huang et al. (2016b) also created the coseismic interferograms of the Meinong earthquake and interpreted this gap as very shallow fault motion. Incidentally, the ALOS-2 interferograms that we used show the same

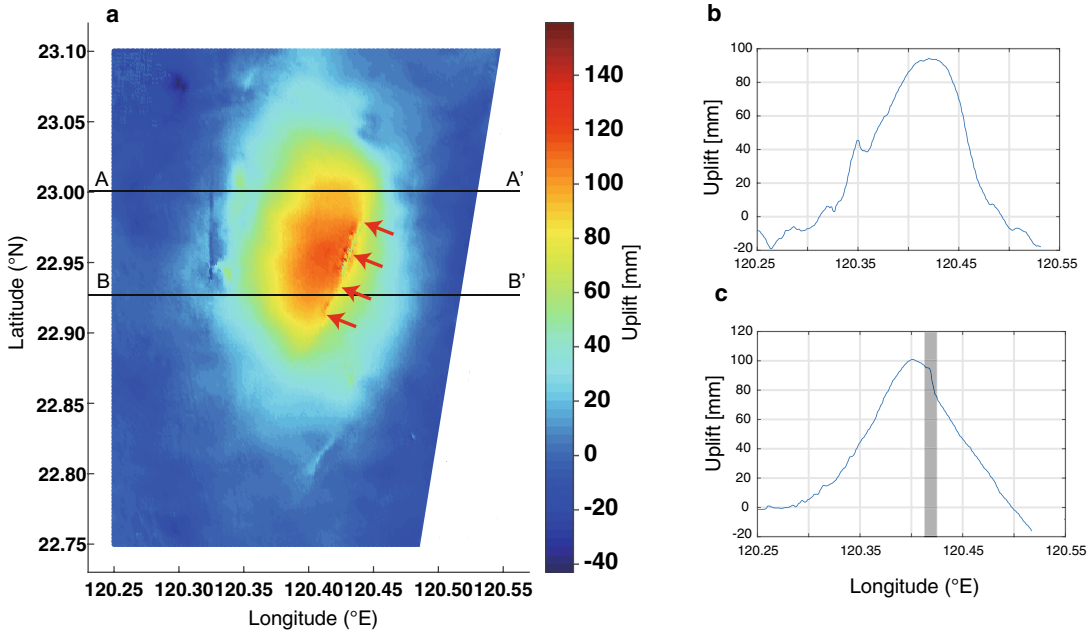

Fig. 4 Coseismic uplift due to the Meinong earthquake measured by ALOS-2. **a** Distribution of coseismic uplift. Gap in the amount of uplift is marked by red arrows. **b** Amount of uplift along the profile A–A′. **c** Amount of uplift along the profile B–B′. Gap in the amount of uplift can be seen and is marked by the shading as well as Fig. 3c. Note that both of the profiles A–A′ and B–B′ are the same as those in Fig. 3

deformation pattern as Sentinel-1 (Huang et al. 2016b). In this study, we demonstrated that this fault slip has aseismically increased at least from 2007 to 2011 when a certain level of shear stress has been statically imposed, as well as at the timing of the Meinong earthquake when a stepwise stress increase is suddenly imposed. Such stable property of the fault slip would be due to the high fluid pressure measured in this area (Huang et al. 2016b). We roughly estimated static Coulomb stress change on the aseismic thrust fault due to coseismic slip of the Meinong earthquake. We assumed slip on the deeper fault of the coseismic fault model proposed by Huang et al. (2016b), which well explains seismic data. We used Coulomb 3.3 to calculate the stress change (Toda et al. 2011). Additional file 1: Figure S8 indicates negative Coulomb stress change on shallower part of the aseismic thrust fault (~ -0.2 MPa), which, as suggested by previous studies (Ching et al. 2016; Huang et al. 2016b), implies that high fluid pressure observed in this area plays important role for triggering slip on the aseismic thrust fault. Thus, the mechanism of interseismic fault creep was confirmed from crustal response to the Meinong earthquake.

It should be noted that the aseismic fault slip we found (Figs. 3, 4) only adds a short-wavelength perturbation to the whole uplift and/or uplift rate pattern. For the interseismic period, the main driving mechanism of whole surface uplift would be mud diapirs at depth. For the coseismic displacement of the Meinong earthquake, a deep-seated decollement caused long-wavelength surface deformation (Huang et al. 2016b), which, however, is not responsible for the interseismic uplift characterized by short-wavelength deformation (Fig. 3).

Conclusion

We detected very rapid uplift along the fold and thrust belt in southwest Taiwan by L-band SAR data. The interferograms are contaminated mainly by ionospheric disturbances, which are corrected by GNSS data. The rapid uplift is aseismically proceeding judging from the absent of earthquakes. The uplift rate increases from south to north and reaches ~ 37 mm/year in the northern part. In southern part, the uplift rate derived from InSAR is consistent with the one measured by the levelling survey which reaches ~ 18 mm/year at maximum. The main cause of uplift motion would be mud diapirs, but we also identified shallow fault motion along the eastern flank of the uplift area, which moves aseismically before and during the 2016 Meinong earthquake. The shallow fault motion adds a short-wavelength perturbation to the whole uplift pattern.

Additional file

Additional file 1. This file contains additional figures of interferograms, fault models, and related information.

Authors' contributions
KT conducted data analysis. KT and YT wrote the manuscript. Both authors read and approved the final manuscript.

Author details
[1] Department of Natural History Sciences, Hokkaido University, N10W8, Kita-ku, Sapporo 060-0810, Japan. [2] Department of Earth and Planetary Sciences, Hokkaido University, N10W8, Kita-ku, Sapporo 060-0810, Japan.

Acknowledgements
We thank Ms. Yoko Tu for discussions. Comments from Yosuke Aoki and an anonymous reviewer greatly improved the manuscript. PALSAR and PALSAR2 data were provided from PIXEL (PALSAR Interferometry Consortium to Study our Evolving Land surface) under cooperative research contract between JAXA and ERI, University of Tokyo. PALSAR data were also provided from JAXA under ALOS-2 PI project. The ownership of PALSAR data belongs to JAXA and METI, Japan. Part of the figures was created by Generic Mapping Tools (Wessel and Smith 1998).

Competing interests
The authors declare that they have no competing interests.

Availability of data and materials
Uplift rates estimated by InSAR are available by requesting the corresponding author by e-mail.

Ethics approval and consent to participate
Not applicable.

Funding
This study was supported by MEXT KAKENHI Grant No. 17K05622, and partly by No. 26400454 to YT.

Publisher's Note

Received: 24 October 2017 Accepted: 14 March 2018
Published online: 26 March 2018

References

Berardino P, Fornaro G, Lanari R, Sansosti E (2002) A new algorithm for surface deformation monitoring based on small baseline differential SAR interferograms. IEEE Trans Geosci Remote Sens 40(11):2375–2383

Ching KE, Gourley JR, Lee YH, Hsu SC, Chen KH, Chen CL (2016) Rapid deformation rates due to development of diapiric anticline in southwestern Taiwan from geodetic observations. Tectonophysics 692:241–251

Doo WB, Hsu SK, Lo CL, Chen SC, Tsai CH, Lin JY, Huang YP, Huang YS, Chiu SD, Ma YF (2015) Gravity anomalies of the active mud diapirs off southwest Taiwan. Geophys J Int 203:2089–2098

Ferretti A, Prati C, Rocca F (2001) Permanent scatterers in SAR interferometry. IEEE Trans Geosci Remote Sens 39(1):8–20

Fruneau B, Pathier E, Raymond D, Deffontaines B, Lee CT, Wang HT, Angelier J, Rudant JP, Chang CP (2001) Uplift of Tainan tableland (SW Taiwan) revealed by SAR interferometry. Geophys Res Lett 28:3071–3074

Fujiwara S, Nishimura T, Murakami M, Nakagawa H, Tobita M (2000) 2.5-D surface deformation of M6.1 earthquake near Mt Iwate detected by SAR interferometry. Geophys Res Lett 27:2049–2052

Fukushima Y, Hooper A (2011) Crustal deformation after 2004 Niigataken–Chuetsu Earthquake, central Japan, investigated by persistent scatterer interferometry. J Geod Soc Jpn 57:195–214 **(In Japanese with English abstract)**

Huang ST, Yang KM, Hung JH, Wu JC, Ting HH, Mei WW, Hsu SH, Lee M (2004) Deformation front development at the northeast margin of the Tainan basin, Tainan–Kaohsiung area, Taiwan. Mar Geophys Res 25:139–156

Huang MH, Hu JC, Ching KE, Rau RJ, Hsieh CS, Pathier E, Fruneau B, Deffontaines B (2009) Active deformation of Tainan tableland of southwestern Taiwan based on geodetic measurements and SAR interferometry. Tectonophysics 466:322–334

Huang MH, Bürgmann R, Hu JC (2016a) Fifteen years of surface deformation in Western Taiwan: insight from SAR interferometry. Tectonophysics 692:252–264

Huang MH, Tung H, Fielding EJ, Huang HH, Liang C, Huang C, Hu JC (2016b) Multiple fault slip triggered above the 2016 Mw 6.4 MeiNong earthquake in Taiwan. Geophys Res Lett 43:7459–7467

Jarvis A, Reuter HI, Nelson A, Guevara E (2008) Hole-filled seamless SRTM data V4. International Centre for Tropical Agriculture (CIAT). http://srtm.csi.cgiar.org. Accessed 10 May 2017

Lin AT, Yao B, Hsu SK, Liu CS, Huang CY (2009) Tectonic features of the incipient arc-continent collision zone of Taiwan: implications for seismicity. Tectonophysics 479:28–42

Massonnet D, Rossi M, Carmona C, Adragna F, Peltzer G, Feigl K, Rabaute T (1993) The displacement field of the Landers earthquake mapped by radar interferometry. Nature 364:138–142

Okada Y (1985) Surface deformation due to shear and tensile faults in a half-space. Bull Seismol Soc Am 75:1135–1154

Rau RJ, Wu FT (1995) Tomographic imaging of lithospheric structures under Taiwan. Earth Planet Sci Lett 133:517–532

Sun CH, Chang SC, Kuo CL, Wu JC, Shao PH, Oung JN (2010) Origins of Taiwan's mud volcanoes: evidence from geochemistry. J Asian Earth Sci 37:105–116

Takada Y, Fukahata Y, Hashima A, Terakawa T, Fukui K, Yanagisawa T, Ikeda Y, Kimura G, Matsu'ura M (2007) Development of three-dimensional basement structure in Taiwan deduced from past plate motion: consistency with the present seismicity. Tectonics 26:TC3004. https://doi.org/10.1029/2006tc001957

Toda S, Stein RS, Sevilgen V, Lin J (2011) Coulomb 3.3 Graphic-rich deformation and stress-change software for earthquake, tectonic, and volcano research and teaching—user guide: U.S. Geological Survey Open-File Report 2011-1060, p 63. http://pubs.usgs.gov/of/2011/1060/

Tsai MC, Yu SB, Shin TC, Kuo KW, Leu PL, Chang CH, Ho MY (2015) Velocity field derived from Taiwan continuous GPS Array (2007–2013). Terr Atmos Ocean Sci 26:527–556

USGS (United States Geological Survey) (2016) M6.4 -25 km SE of Yujing, Taiwan. https://earthquake.usgs.gov/earthquakes/eventpage/us20004y6h#executive Accessed 10 May 2017

Wegmüller U, Werner C (1997) Gamma SAR processor and interferometry software. In: Proceedings of the 3rd ERS symposium European space agency, Spec Publ, pp 1687–1692

Wessel P, Smith WHF (1998) New, improved version of generic mapping tools released. EOS Trans Am Geophys Union 79:579. https://doi.org/10.1029/98EO00426